

Printable Fabrication of a Fully Integrated and Self-Powered Sensor System on Plastic Substrates

Yuanjing Lin, Jiaqi Chen, Mohammad Mahdi Tavakoli, Yuan Gao, Yudong Zhu, Daquan Zhang, Matthew Kam, Zhubing He, and Zhiyong Fan*

Wearable and portable devices with desirable flexibility, operational safety, and long cruising time, are in urgent demand for applications in wireless communications, multifunctional entertainments, personal healthcare monitoring, etc. Herein, a monolithically integrated self-powered smart sensor system with printed interconnects, printed gas sensor for ethanol and acetone detection, and printable supercapacitors and embedded solar cells as energy sources, is successfully demonstrated in a wearable wristband fashion by utilizing inkjet printing as a proof-of-concept. In such a “wearable wristband”, the harvested solar energy can either directly drive the sensor and power up a light-emitting diode as a warning signal, or can be stored in the supercapacitors in a standby mode, and the energy released from supercapacitors can compensate the intermittency of light illumination. To the best of our knowledge, the demonstration of such a self-powered sensor system integrated onto a single piece of flexible substrate in a printable and additive manner has not previously been reported. Particularly, the printable supercapacitors deliver an areal capacitance of 12.9 mF cm⁻² and the printed SnO₂ gas sensor shows remarkable detection sensitivity under room temperature. The printable strategies for device fabrication and system integration developed here show great potency for scalable and facile fabrication of a variety of wearable devices.

Wearable and portable devices contribute to a rapidly growing emerging market for electronics and can find wide applications for wireless communications, multifunctional entertainments, personal healthcare monitoring, etc.^[1–5] Typically, wearable devices with attractive attributes such as flexibility, long cruising time, and operation safety are highly desirable.^[6–11] Recent advances in fields of power generation devices enable sustainable energy harvesting from the environment, such as solar energy, mechanical vibrations and frictions, biofluid and thermal energy from human body, and converted into electricity without external power sources, which introduces the concept of “self-powered” systems.^[12–17] To realize continuous operation of the entire self-powered devices without interruption from surrounding conditions variation, such as insufficient solar illumination, fully integrated self-powered systems that consist of energy harvesting/conversion devices (e.g., solar cells, nanogenerators, biofuel cells), energy storage devices as intermediate energy storage units (e.g., rechargeable batteries, supercapacitors)

and functional devices (e.g., sensors, transistors, biomedical implants) are highly desirable.^[18] Planar supercapacitors with interdigitated electrodes constructed on single substrate emerged as one of the highly competitive energy storage devices to complement/replace batteries, offering merits of high power density, separator-free architectures for device miniaturization, and favorable operational safety without using flammable electrolytes.^[19–22] Especially for integration with energy harvesting devices dealing with highly volatile energy input, particularly in wearable applications, supercapacitors possess an appealing capability to accommodate fast and high charging current fluctuation.^[23–26] Although self-sufficient energy modules (e.g., photovoltaic-batteries, nanogenerator-supercapacitors) and self-powered sensors (e.g., nanogenerator-sensors, battery-sensors) have been reported previously,^[12,23,26–32] to our best knowledge, demonstration of a fully integrated self-powered sensor system on flexible substrate implemented via additive printable strategy is rarely achieved, mainly due to the challenges on fabrication procedures compatibility and system integration of different device components.

Y. Lin, Dr. J. Chen, Dr. M. M. Tavakoli, Dr. Y. Gao,^[†] Y. Zhu, D. Zhang, M. Kam, Prof. Z. Fan

Department of Electronic and Computer Engineering
The Hong Kong University of Science and Technology
Clear Water Bay, Kowloon, Hong Kong SAR, China
E-mail: eezfan@ust.hk

Dr. M. M. Tavakoli
Department of Electrical Engineering and
Computer Science Massachusetts Institute of Technology
MA 02139, USA

Y. Zhu, Prof. Z. He
Department of Materials Science and Engineering
Shenzhen Key Laboratory of Full Spectral Solar Electricity Generation
(FSSEG)
Southern University of Science and Technology
No. 1088, Xueyuan Rd, Shenzhen, Guangdong 518055, China

 The ORCID identification number(s) for the author(s) of this article can be found under <https://doi.org/10.1002/adma.201804285>.

^[†]Present address: Institute of Textiles and Clothing, The Hong Kong Polytechnic University, Hong Kong SAR, China

DOI: 10.1002/adma.201804285

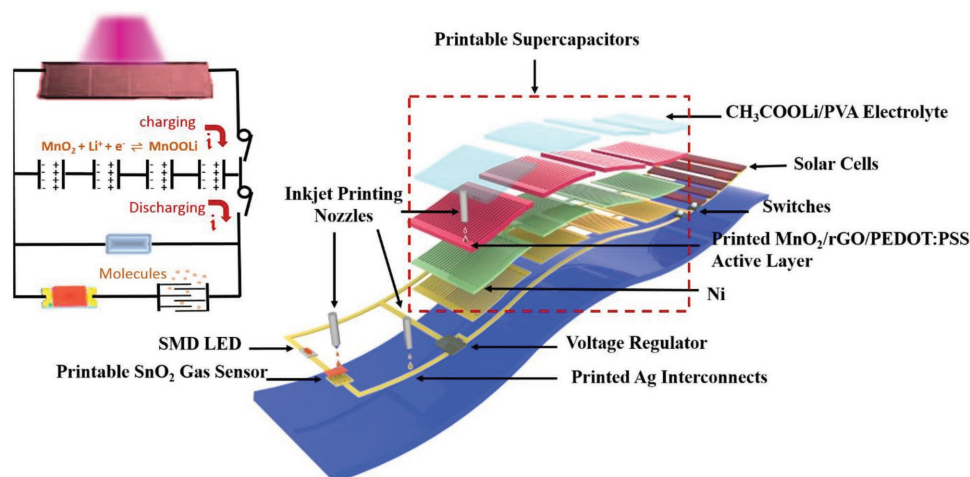


Figure 1. Schematic images of printable fabrication procedures and system operational mechanism (inset) of the flexible and wearable monolithically integrated self-powered smart sensor system on plastic substrate.

Herein, we demonstrated a printable fabrication approach to construct a self-powered sensor system for gas detection in a wearable wristband fashion, and it is the first report on monolithic integration of such a system on a piece of flexible plastic substrate in ambient environment by utilizing additive inkjet printing technique. Such a “wearable wristband” mainly consists of printed silver (Ag) interconnects, amorphous silicon (a-Si) solar cells array as energy harvesting and conversion module, planar MnO_2 -based supercapacitors as intermediate energy storage devices, and SnO_2 gas sensor with a light-emitting diode (LED) indicator as active and power consumption units. The harvested solar energy can either directly drive the sensor and light up the LED indicator, or can be stored in supercapacitors in a standby mode and the energy released from supercapacitor can compensate the intermittency of illumination. It is worth mentioning that the whole system is designed into a planar architecture for monolithic integration, including both planar supercapacitors and sensor with interdigitated electrodes. Several kinds of inks were adopted to realize printable fabrication of such a system, including interconnects, supercapacitors, and gas sensor. Particularly, different functional nanoparticles were synthesized and prepared into stable inks with modified solvent systems. Note that ink modification is highly critical for fabrication of printable devices with decent performances. For instance, unstable inks with large particle clusters will cause nozzle clogging during inkjet printing process and result in relatively low device yields. With the novel and optimized hybrid ink consists of Manganese(IV) oxide (MnO_2)/reduced graphene oxide (rGO)/poly(3,4-ethylenedioxythiophene):poly(styrene sulfonate) (PEDOT:PSS), the as-printed planar supercapacitors presented an areal capacitance of 12.9 mF cm^{-2} . As an application demonstration, a fully printed SnO_2 gas sensor in a chemiresistor format was utilized for ethanol and acetone detection. Notably, ethanol detection is essential for drunk-driving tests and acetone is one of the biomarkers for diabetes clinical diagnostics, and continues noninvasive monitoring of the status of diabetes patients are highly desired.^[1,33] The as-printed SnO_2 gas sensor showed remarkable sensitivity under room temperature, and the

corresponding drop of the sensor resistance enables the LED to light up and send out a warning signal. It is also worth mentioning that as a maskless, noncontact and drop-on-demand printing technique,^[34] the utilization of inkjet printing not only provides scalable and versatile fabrication approaches for device fabrication in an additive manner, but also enables facile and monolithic integration of different types of device units on flexible substrates in ambient. The methodology developed in this work demonstrates a practical potency in a variety of wearable integrated self-powered devices for applications in healthcare, biomedical monitor, and intelligent robotics, etc.^[35,36]

The printable fabrication procedures of such a monolithically integrated system on flexible substrate are schematically shown in **Figure 1** with more technical details provided in the Experimental Section. Briefly, the circuit interconnects and electrode patterns for both planar supercapacitors and sensor were inkjet printed with Ag nanoparticle colloidal ink onto the porous poly(ethylene terephthalate) (PET) substrate (Figure S1a, Supporting Information), followed by electroless plating of nickel (Ni) onto Ag electrode patterns to form stable current collectors for supercapacitors (Figure S1b1, Supporting Information). Pseudocapacitive MnO_2 -based hybrid ink was then inkjet printed onto the as-fabricated current electrodes in a drop-on-demand fashion (Figure S1b2, Supporting Information). To realize solid-state supercapacitors, 1 M lithium acetate/poly(vinyl alcohol) ($\text{CH}_3\text{COOLi/PVA}$) gel was utilized as electrolyte and drop-casted onto the surface of as-printed interdigitated electrodes. Meanwhile, SnO_2 ink was also inkjet printed on the Ag electrodes to achieve a fully printed gas sensor (Figure S1b, Supporting Information). Afterwards, a-Si solar cells and other supporting electronic components, including surface mounted (SMD) LED, voltage regulator and switches, were mounted onto printed Ag interconnects to realize a self-powered sensor system on a single piece of PET (Figure S1c, Supporting Information).

As shown in the inset schematic figure in Figure 1, in such a self-powered system, energy harvesting is realized with a-Si solar cells array which converts light into electricity. Under light condition, the energy required for gas detection with LED

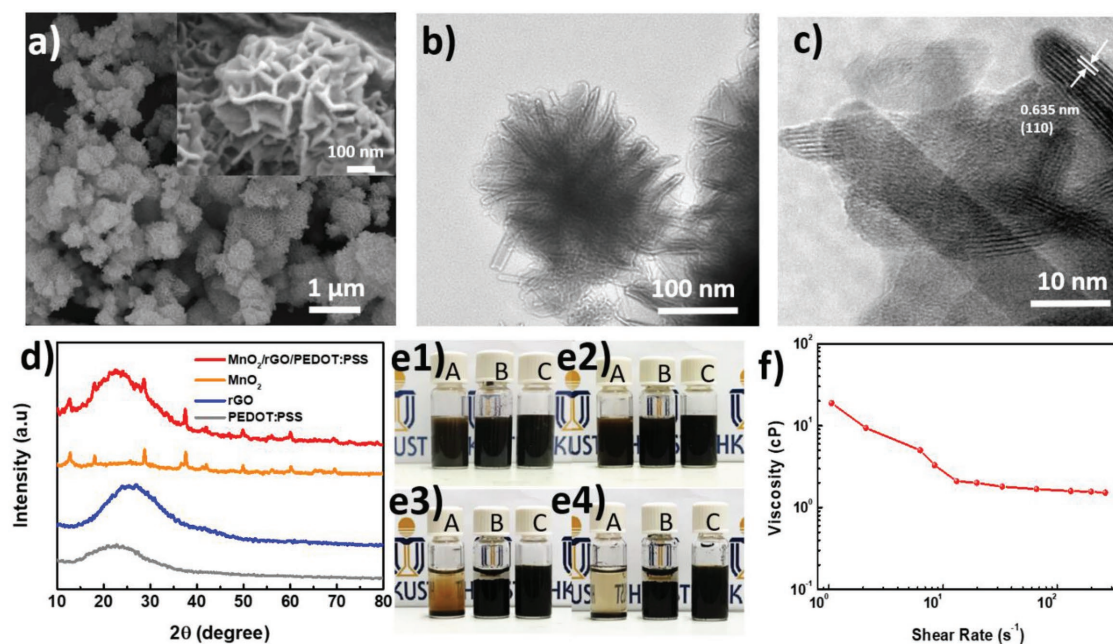


Figure 2. Characterizations of printable $\text{MnO}_2/\text{rGO}/\text{PEDOT:PSS}$ hybrid ink. a) SEM images and b,c) TEM images of MnO_2 nanoparticles fabricated via hydrothermal method. d) XRD spectra of $\text{MnO}_2/\text{rGO}/\text{PEDOT:PSS}$ hybrid ink and each composites. e) Photographs of the different inks (A: MnO_2 aqueous ink; B: MnO_2/rGO aqueous ink; C: $\text{MnO}_2/\text{rGO}/\text{PEDOT:PSS}$ aqueous ink) kept on shelf over time. Images were taken (e1) immediately after preparation, (e2) after 10 min, (e3) after 12 h, and (e4) after 5 d. f) Viscosity of $\text{MnO}_2/\text{rGO}/\text{PEDOT:PSS}$ ink as a function of shear rate.

warning signal can be directly supplied with the solar cells array. Alternatively, the converted photocurrent can also charge up the printable supercapacitors, which are connected in series to provide adequate operational voltage window, and released to support system function in dark condition. As the voltage output of the solar cells or supercapacitors might fluctuate during operation, for example when the user wearing the device is moving physically, a voltage regulator is introduced to stabilize the voltage applied on the gas sensor and mounted LED. With detection of ethanol and acetone, the corresponding drop of the sensor resistance results in an increased voltage applied on the LED so as to light up as a warning signal (Figure S1d, Supporting Information).

To realize printable planar supercapacitors with decent performance and ensure a smooth fabrication process without clogging of printing nozzles, synthesis of functional nanomaterials together with modification of solvent systems are critical to achieve printable inks with desirable viscosity, proper concentration, and high stability, etc.^[37,38] In this work, MnO_2 with merits of low-cost, high theoretical capacitance was utilized as pseudocapacitive material, and MnO_2 nanoparticles with an average size of around 500 nm were synthesized via hydrothermal method,^[39,40] as shown in the scanning electron microscope (SEM) images in Figure 2a. The Mn^{4+} ion was indicated in X-ray photoelectron spectroscopy (XPS) (Figure S2a, Supporting Information) and the energy dispersive spectrometer (EDS) images are shown in Figure S2b–d in the Supporting Information. The as-synthesized MnO_2 nanoparticles have a highly porous surface morphology as shown in both high-resolution SEM image (inset of Figure 2a) and transmission electron microscopy (TEM) image (Figure 2b), which is a nature outcome of the entangled nanowires coming into formation

during the hydrothermal reaction. As shown in Figure 2c, the as-synthesized MnO_2 nanoparticles are well crystallized with a lattice distance of 0.635 nm that corresponds to the (110) lattice face in $\alpha\text{-MnO}_2$, which was also characterized by X-ray diffraction (XRD) spectrum as shown in Figure 2d.

Though the well-crystallized nanoparticles can deliver improved electrical conductivity compared with those in poor crystallinity, the MnO_2 itself as metal oxide still has relative large impedance.^[41] In this regard, rGO nanoflakes were introduced as conductive binder and itself also provides large surface area for charge storage. Notably, PEDOT:PSS as conductive polymer was found to be a suitable additive to achieve stable ink with proper viscosity. The XRD spectra of $\text{MnO}_2/\text{rGO}/\text{PEDOT:PSS}$ hybrid ink (Figure 2d) indicate no chemical reaction among the ink composites. As shown in Figure 2e, the stability of hybrid ink with PEDOT:PSS is significantly improved and no precipitation separation was observed for over 5 d on shelf. Besides, the as-prepared ink shows a shear behavior with a viscosity of around 12 cP at the shear rate of 1 s^{-1} , which is suitable for inkjet printing (Figure 2f).^[34] Such a novel hybrid printable ink with suitable nanoparticle sizes, excellent stability, and proper viscosity ensures the smooth inkjet printing process and contributes to the decent performance of printable supercapacitors.

The architecture of the supercapacitor electrodes fabricated with the hybrid ink is schematically illustrated in Figure 3a. The rGO nanoflakes form into a conductive network with large surface area for MnO_2 nanoparticles loading. This hierarchical structure provides necessary porosity for electrolyte ion diffusion, shortening electron transfer pathways, and prevent delamination of these nanoparticles into electrolyte.^[42,43] The construction of such supercapacitor electrodes starts from the printed Ag interdigitated fingers pattern, with a finger width

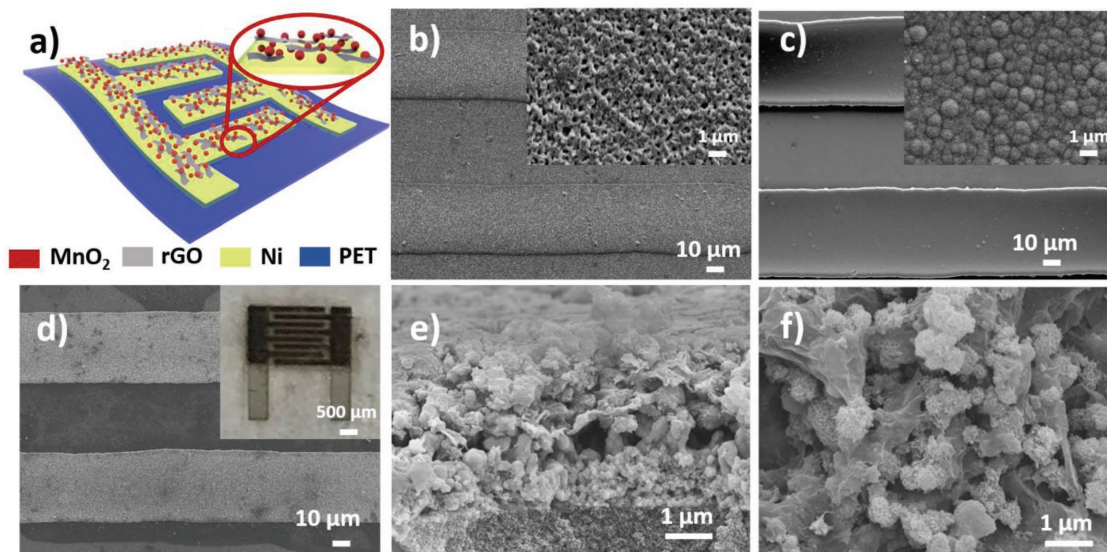
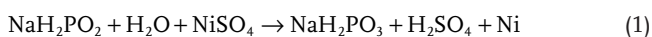


Figure 3. Device structure of printable planar supercapacitors. a) Schematic image of printable planar supercapacitor device with MnO₂/rGO hierarchical structures. b–d) Top view SEM images of inkjet-printed Ag electrode patterns with certain surface roughness (inset: high-resolution SEM image) (b), electroless plating of Ni on Ag patterns to achieve stable current collectors (inset: high-resolution SEM image) (c), and the as-printed MnO₂/rGO supercapacitor electrodes (inset: photograph of as-printed device) (d). e, f) High-magnitude SEM images of cross-section (e) and top view (f) of the supercapacitor electrodes with MnO₂/rGO hierarchical structures.

and interspace between neighboring fingers of $\approx 50 \mu\text{m}$ respectively, as shown in Figure 3b. Note that the pattern resolution can be narrowed down to a minimized interspace of $5 \mu\text{m}$ for further enhancement on performance, which has been reported in our previous works.^[42] Since Ag tends to be oxidized in aqueous electrolytes when a potential is applied and fails to function as stable current collectors, Ni layers were further deposited on the surface following a classic and scalable electroless plating method, utilizing nickel(II) sulfate (NiSO₄) as Ni source and sodium hypophosphite (NaH₂PO₂) as reductant without applying external electric current.^[44–46] As shown in the SEM images in Figure 3c and EDS mapping images (Figures S3 and S4, Supporting Information), uniform Ni layers with a thickness of around $1 \mu\text{m}$ only form on the Ag patterned areas. We proposed that the printed Ag layer with certain roughness serves as a preferred nucleation sites than blank PET substrates for the initial reduction of Ni²⁺ in heated electrolyte. Afterwards, the electroless plating process occurs on the active catalytic surface of Ni following Equation (1)^[44,45]



The crystallization of the as-deposited Ni thin film on printed Ag pattern was confirmed by the XRD spectrum, as shown in Figure S5 in the Supporting Information. To realize supercapacitor electrodes, the MnO₂/rGO/PEDOT:PSS hybrid ink was then directly inkjet printed for five cycles on top of Ni (Figure 3d), with an average thickness of around $2.5 \mu\text{m}$ (Figure 3e). As shown in Figure 3f, the as-printed electrodes show a hierarchical architecture with rGO interconnected conductive network loaded with MnO₂ nanoparticles.

Systematic study on performance optimization and evaluation of the as-fabricated printable planar supercapacitors

(inset photo in Figure 3d) was performed in this work. Note that for a planar supercapacitor, the mass loading of electrode materials is normally very small compared with the entire device, thus the volumetric/areal capacitances are considered as more important figure-of-merits than gravimetric capacitance.^[19] In general, the overall capacitance of the device is largely determined by the active materials mass loading and the conductivity of the electrodes.^[42] Specifically in this work, the supercapacitor capacitance comes from the MnO₂/rGO/PEDOT:PSS hybrid ink. As PEDOT:PSS mainly serves as an additive to stabilize the printable ink, the amount is negligible and so is its contribution to the capacitance. Thus, the ratio between MnO₂ and rGO plays a critical role for the supercapacitors. Due to the fact that rGO stores energy by physical ion adsorption, it delivers relatively small capacitance compared with MnO₂ of same amount, which is also involved in redox reaction for charge storage.^[47] Though the electrode conductivity can be successively improved with larger ratios of rGO, the specific capacitance of device might not be in a monotonic increasing tendency. Therefore, printable inks with different ratios of MnO₂ and rGO, ranging from pure MnO₂ to 5:1 (MnO₂:rGO w:w) were prepared for device performance optimization. For fair comparisons, same printing parameters, including printing cycles and space between droplets were applied for fabrication of supercapacitor devices with different printable inks.

To evaluate the electrochemical performance of the printable solid-state planar supercapacitors, cyclic voltammetry (CV) measurements at a scan rate from 5 to 100 mV s^{-1} were tested, together with galvanostatic charging–discharging (GCD) measurements at a current density from 0.17 to 0.51 mA cm^{-2} , with a voltage range from 0 to 0.8 V . The corresponding CV curves of the devices fabricated with printable inks in different

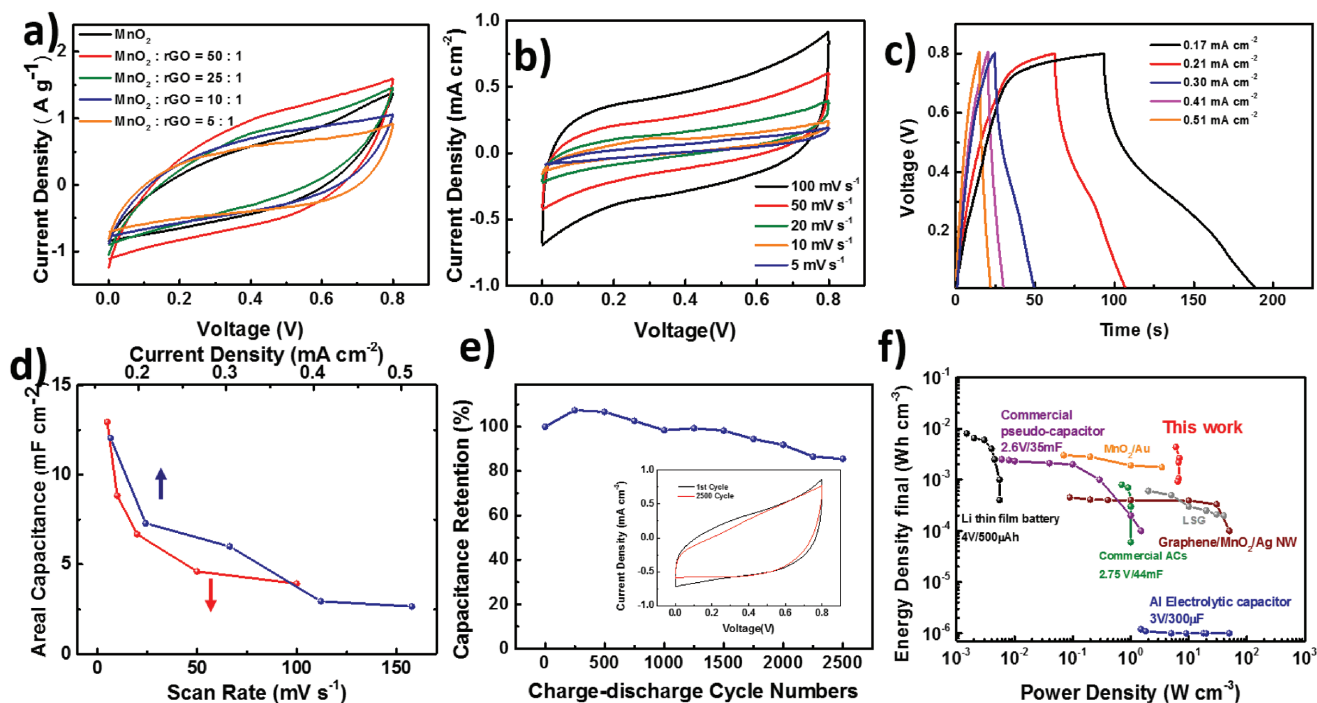


Figure 4. Performance evaluations of printable supercapacitors. a) CV curves of electrodes printed with inks in different MnO_2/rGO ratios recorded at scan rates of 10 mV s^{-1} . b) CV curves of the planar supercapacitor devices with optimized ink formulation ($\text{MnO}_2/\text{rGO} = 50:1$) recorded at scan rates of 5, 10, 20, 50, 100 mV s^{-1} . c) GCD curves of the planar supercapacitor devices with optimized ink formulation at a discharge current of 0.17, 0.21, 0.30 and 0.41, 0.51 mA cm^{-2} . d) Areal capacitance of device calculated from CV and GCD measurement, respectively. e) Cycling stability test of device at a scan rate of 100 mV s^{-1} . Inset: CV curves at the 1st cycle and after 2500 cycles. f) Ragone plots show the energy density and power density of the device, in comparison of the other energy storage devices.

ratios of MnO_2 and rGO are shown in **Figure 4a**. It is obvious from the CV curves that the electrodes achieve the highest areal capacitances at the optimized ratio of 50:1 (MnO_2/rGO), with rate performances shown in **Figure S6a** in the Supporting Information. The SEM images of as-printed electrodes (**Figure S6b–f**, Supporting Information) indicate that the performance enhancement can be attributed to two reasons: (1) The charge transfer is facilitated with the rGO network, which was also confirmed by electrochemical impedance spectroscopy (EIS) measurements, as shown in **Figure S7** in the Supporting Information. The largest radius of the semicircle in the high-frequency region indicates that the electrode printed with pure MnO_2 ink has the largest charge transfer impedance, resulted from the high resistance of MnO_2 itself.^[41] In contrast, the radius of semicircle in EIS curves decreases with the increased ratios of rGO in the printable inks. (2) The rGO hierarchical networks loaded with satellite MnO_2 nanoparticles increase the surface area for charge storage and electrolyte ion contact for more completed redox reaction of MnO_2 .

The optimized device performance is also indicated both by the quasi-rectangular CV curves with negligible shape distortion at the increasing scan rate (**Figure 4b**) and the GCD curves that exhibit a highest coulombic efficiency of 95.5% (**Figure 4c**). Note that for the as-printed active layers with thickness in micrometer scale, the effect of intercalation and deintercalation of metal alkali ion into/out of the sublayer of MnO_2 will become more obvious with smaller currents for slow charge-discharge processes. In this case, a small discharging voltage

plateau can be observed. The highest areal capacitance achieved is 12.9 mF cm^{-2} at the scan rate of 5 mV s^{-1} and 12.2 mF cm^{-2} at the discharging current density of 0.17 mA cm^{-2} (**Figure 4d**). And such respectable values are considerably high when compared with previous reports on printable planar supercapacitors. Besides, the stability of the as-fabricated devices was verified by cyclic life measurement conducted at the scan rate of 100 mV s^{-1} (**Figure 4e**). The capacitance increase can be observed during the initial cycles, which could be attributed to the activation of the materials.^[48] Afterwards, the capacitance tends to be stable and maintains over 80% of its capacitance after 2500 cycles of measurement. The capacitance degradation can result from the reduced contact between MnO_2 and rGO during the charging-discharging cycling process accompanied with volume expansion, and the delamination of active materials into electrolyte.^[42]

The specific energy and specific power of the as-fabricated printable planar supercapacitor are compared with commercial products and the relevant works, as shown in the Ragone plot (**Figure 4f**). The device printed with $\text{MnO}_2/\text{rGO}/\text{PEDOT:PSS}$ hybrid ink exhibits the highest specific energy of 4.5 mWh cm^{-3} , which is quite competitive compared with several reported works in fields of planar/printable supercapacitors^[49–51] and demonstrates four orders of magnitude improvement than that of aluminum electrolytic capacitors (3 V/300 μF). The highest specific power achieved by the device is 7.2 W cm^{-3} , which is over three orders of magnitude higher than that of the reported commercial lithium thin film battery (4 V/500 μAh). Moreover, the as-printed supercapacitors have a superior energy storage

capability compared with commercial activated carbon based supercapacitors (2.75 V/44 mF) and commercial pseudocapacitor (2.6 V/35 mF).

As a function demonstration, a SnO₂ gas sensor was fabricated onto the system in a fully printable manner. SnO₂ as a n-type semiconductor, is one of the most commonly used material for gas sensing mainly due to its low cost, stability, and repeatability.^[52] While metal oxide sensors normally require high operation temperature (over 200 °C) to achieve high sensitivity and fast recovery, recent studies demonstrated the SnO₂ has the capability for volatile organic compounds detection under room temperature, which eliminate the integration of heaters and thermal isolation units.^[53,54] Especially for portable and wearable electronics, room temperature operational sensors are highly desirable for device miniaturization and long cruising time without extra power consumption for heaters.^[53] As gas sensing is a surface reaction dominated process, the material morphology and uniformity have large influence on the sensor performance.^[55] In this regard, inkjet printing technique enables the deposition of a uniform film with controllable thickness.

To realize printable sensors, SnO₂ nanoparticles were first obtained through the hydrothermal method with a grain size of around 30 nm for printable ink preparation,^[56] as shown in the TEM images in Figure S8 in the Supporting Information. Such nanoparticles will contribute to both the improved sensitivity with high surface area to volume ratio, and smooth printing process without nozzles clogging issue. The as-synthesized SnO₂ nanoparticles were then suspended in ethanol and ultrasonicated for 30 min to form a colloidal printable ink (inset of Figure 5a). A typical XRD pattern of a printed SnO₂ layer with the as-prepared ink is shown in Figure 5a, with dominant peaks at 26.49°, 33.75°, and 51.74° corresponding to (110), (101), and (211), indicating the tetragonal rutile phase of SnO₂

nanoparticles. Notably, it has been reported that the adsorption of ethanol and acetone on surface facets of (110) and (101) is thermodynamically favorable, and thus the as-printed SnO₂ thin films is suitable for gas detection.^[54] As shown in the SEM and EDS images (Figure 5b,c; Figure S9, Supporting Information), the inkjet printed SnO₂ layer is uniform and continuously bridges the Ag integrated electrodes with an electrode width of 50 μm and interspace of 100 μm.

The as-printed sensors were located in the test chamber and measured under room temperature (25 °C) and atmospheric pressure (101.3 kPa). The target gas (i.e., ethanol and acetone) concentrations were controlled by two programmable mass flow controllers (MFCs) to adjust the ratios of gas vapor and dry air (carrier gas), with a constant flow rate of 500 sccm. The resistances (*R*) of sensors were continuously monitored, and more details can be found in the Experimental Section. According to the ionosorption mechanism, when the sensors are initially exposed to dry air, oxygen molecules adsorb on the surface of SnO₂ and capture free electrons.^[54] These electrons will then be released back to SnO₂ when reduction gas (e.g., ethanol, acetone) is introduced into the system and interacts with oxygen species. Thus, the resistance of SnO₂ decreases with detection of ethanol or acetone. Figure 5d,e show the response of the fully printable SnO₂ gas sensors towards a large range of ethanol and acetone concentration and fast recovery within several mins. In general, higher concentration of target gas leads to a larger sensor resistance decrease as expected. The normalized sensitivity (*S*) of the sensors is defined as Equation (2)

$$S = \frac{|\Delta R|}{R_0} = \frac{|R_g - R_0|}{R_0} \times 100\% \quad (2)$$

where *R_g* is the resistance of sensor with detection of target gas and *R₀* is the initial resistance. As shown in Figure 5f, the fully

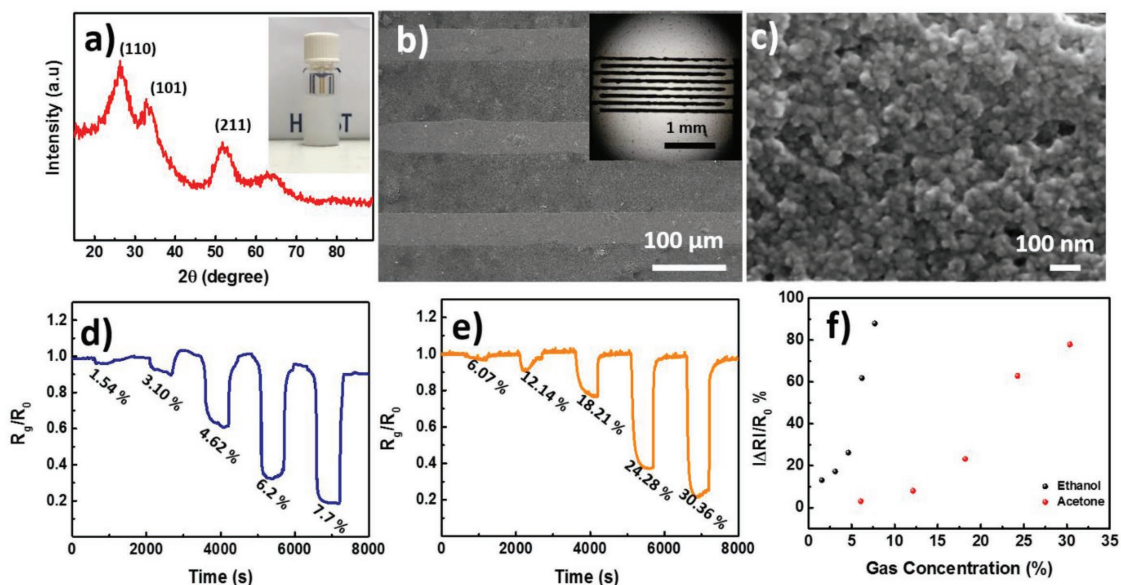


Figure 5. Characterizations and performance evaluations of printable SnO₂ gas sensors. a) XRD spectrum of inkjet printed SnO₂ layer. Inset: Photo of printable SnO₂ ink. b) SEM and the optical microscopy (inset) images of the as-printed sensor. c) High-magnitude SEM image of as-printed SnO₂ layer. d,e) Response of as-printed sensor towards ethanol (d) and acetone (e) under room temperature. f) Sensor sensitivities as a function of target gases concentrations.

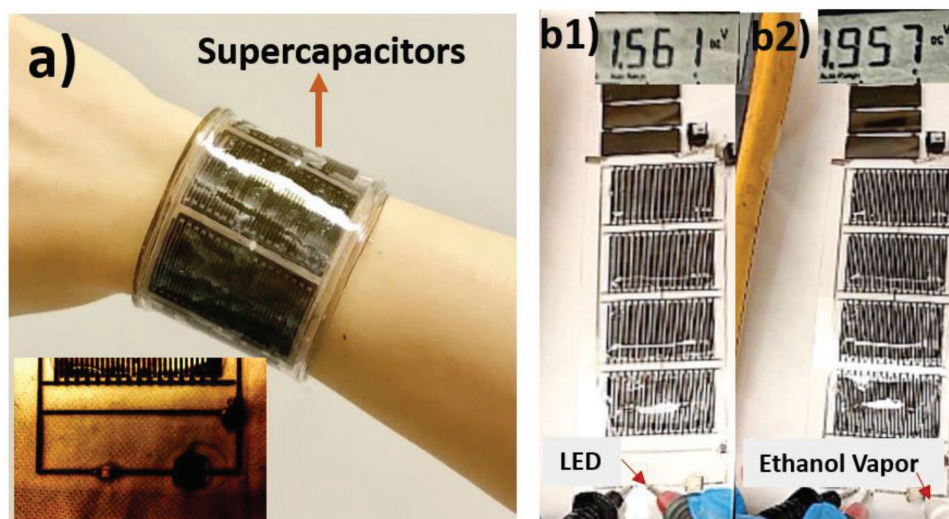


Figure 6. Demonstration of monolithically integrated self-powered sensor system. a) Photos of wearable wristband. Inset: LED as the indicator of gas detection. b) Voltage drop on LED (b1) without and (b2) with detection of ethanol in ambient. Inset: Voltage values read on multimeter.

printed SnO_2 sensors delivered a sensitivity of 13.2% to 1.54 vt % of ethanol, and 3.1% to 6.07 vt % of acetone. Notably, due to the fact that the hydroxyl group has stronger interact with SnO_2 surface,^[54] the sensors show higher sensitivity to ethanol while superior recovery performances are observed as for acetone detection.

With the high scalability and versatility of the as-developed printable fabrication approach, a fully and monolithically integrated self-powered system in the size of $15.0 \text{ cm} \times 4.0 \text{ cm}$ was successfully constructed on a single PET substrate with programmable patterns, and can be packaged into a flexible and wearable wristband fashion with poly(dimethylsiloxane) (PDMS), as shown in **Figure 6a**. Under normal table lamp illuminance (8 W white light), the 4×5 array of commercial a-Si solar cells can provide an output voltage of 2.8 V. When switching on photo charging function, the large scale supercapacitors (single device area of 5.9 cm^2) connected in series can be quickly charged up in a rate of 150 mV min^{-1} , and maintained an operational voltage of over 1.6 V for more than 1 min as a single power supply unit (see Movie S1 in the Supporting Information). The voltage applied on the SnO_2 gas sensor and mounted LED was stabilized by the voltage regulator with an upper limit of 2.75 V. As shown in **Figure 6b**, when the system is exposed to ethanol or acetone, the resistance drop of SnO_2 sensor results in the voltage applied on LED rising from 1.56 to 1.96 V (also see Movie S2 in the Supporting Information). Therefore, the LED can be turned on as a warning signal, as shown in the inset photo of **Figure 6a**. As the first concept demonstration of such a monolithically and fully integrated self-powered sensor system realized in a printable approach, performance enhancement can be expected for further optimization on single device units and system functional stability. For instance, the conductivity of the as-printed Ag interconnects can be enhanced with other commercially available inks that provide even higher conductivity, while the cost will increase, to be competitive with those on conventional printed circuit boards (**Figure S10**, Supporting Information). On the other hand, the system demonstrated in

this work is operated in a low-power mode, and thus the power consumption on interconnects is nearly negligible. Also, sensors with higher sensitivity can be realized with strategies such as nanoengineering by applying 3D porous templates or surface decoration with noble metal nanoparticles.^[53,57,58] Recent studies also demonstrate the strategies to achieve flexible solar cells (e.g., perovskite solar cells) in printable manners with novel device structures and combination of different printing techniques,^[34,59] and thus a fully printable and wearable self-powered fabricated on flexible substrate is also promising.

Printable electronics has emerged as a new class of devices complementing those manufactured by conventional technologies, such as lithographic technique based silicon electronics, mainly due to its relatively facile and low cost fabrication procedures, as well as desirable scalability and versatility in device designs.^[60–62] Although rapid advances in printable devices (e.g., transistors, batteries) have been witnessed in recent years,^[34,38,63] extensive research efforts are still required in the synthesis of printable materials for a variety of functional devices and the realization of fully printable electronics for practical applications. In this work, the concept of a printable and wearable self-powered sensor system for ethanol/acetone detection was demonstrated, and it is the first report on a monolithically and fully integrated system that was successfully constructed on flexible plastic substrate in ambient environment by utilizing additive inkjet printing. Such a wearable wristband mainly consists of inkjet printed electrical interconnects, a-Si solar cells for energy harvesting/conversion, printable MnO_2 -based planar supercapacitors for energy storage and fully printable SnO_2 gas sensor for ethanol/acetone detection. With the supercapacitors serving as photovoltaic energy storage units and providing power for the functional devices during intermittent light illumination, simultaneous functionality without external charging modules can be realized, which is highly desirable for wearable and portable electronics. Notably, different functional nanoparticles were synthesized and prepared into printable inks for the fabrication of supercapacitors and gas sensors.

With the novel modification in the solvent system, the MnO₂/rGO/PEDOT:PSS ink shows enhanced stability and the as-fabricated planar supercapacitors delivered an areal capacitance of 12.9 mF cm⁻². As a functional demonstration, the SnO₂ gas sensor showed remarkable sensitivity towards ethanol/acetone and the resulted resistance drop turns on the LED as a warning signal. The printable fabrication methodology developed in this work demonstrates its facileness and scalability for both device fabrication and system integration, and such a concept demonstration of a printable integrated self-powered sensor system can inspire future additive fabrication of a wide variety of wearable and portable devices, especially for personalized healthcare, biomedical monitor applications.

Experimental Section

Chemicals and Commercial Electronics: All the chemicals were of reagent grade. The a-Si solar cells were ST-2509-4 series. The supporting electronic devices including a MIC5231-2.75YM5 voltage regulator and a surface mounted LED (0603).

Design and Printing of the Patterns and Interconnects for the Integrated System: The patterns with interdigitated electrode fingers were first designed in computer painting program and then imported to the software of Dimatrix Material Printer (DMP 2831, FUJIFILM). The patterns were then printed on PET-based substrate (Novole IJ-220, NovaCentrix) with Ag ink (Metalon JS-B25HV, NovaCentrix) and annealed at 60 °C for 30 min to evaporate the solvent. The line widths for the interconnects are around 700 μm. The electrode width and interspace for the large scale planar supercapacitors are both 500 μm, with a device area of 2.15 cm × 2.75 cm. The electrode width for the gas sensor integrated in the system are 200 μm with interspace of 300 μm, and the length of electrodes are 7 mm.

Synthesis of MnO₂/rGO/PEDOT:PSS Ink: The MnO₂ nanoparticles were synthesized through a hydrothermal method. 1.25 g potassium permanganate (KMnO₄) and 0.6148 g manganese(II) chloride tetrahydrate (MnCl₂·4H₂O) were added in 80 mL deionized (DI) water and kept in 80 °C water bath with stirring for 4 h. After that, the particles were then washed with DI water for three times and annealed in 250 °C for 48 h in oven. 100 mg of the as-prepared MnO₂ particles, 6.5 mg of PEDOT:PSS were then mixed with rGO (in different weight ratios of MnO₂/rGO) in 4 mL DI water. The mixture was then sonicated under 100 W with 50% duty cycle for 5 min (Branson Sonifier 250) to achieve a homogeneous solution for printing.

Electroless Planting of Ni: The electroless plating electrolyte consisted of 4 g nickel sulfate (NiSO₄), 5.9 g sodium citrate (Na₃C₆H₅O₇), 3.2 g ammonium chloride (NH₄Cl), and 2.7 g sodium hypophosphite (NaH₂PO₂) in 84 mL DI water. The electrolyte was tuned to a pH of around 8.5–9 with ammonia solution (28%) and kept in 85 °C water bath. The sample was then immersed into the electrolyte for 30 min and a Ni layer with a thickness of around 1 μm can be achieved.

Assembling of All-Solid-State Planar Supercapacitors: 12 g PVA and 12 g 85 wt % CH₃COOLi were dissolved in 120 mL DI water. After that, the solution was vigorously stirred at 85 °C until it became clear. Then, the solution was cooled down to room temperature and used as a gel electrolyte. The electrolyte was drop casted on the interdigitated electrodes and was kept in air for 24 h to make it an all-solid-state planar supercapacitor.

Synthesis of SnO₂ Ink: SnO₂ nanoparticles were prepared through a hydrothermal method. 99% tin chloride pentahydrate (SnCl₄·5H₂O) was dissolved in DI water with a concentration of 3 wt %. To enforce the hydrolyzation process and produce tin hydroxide (Sn(OH)₄), 15 mL ammonia solution (28%) was added to a 15 mL SnCl₄ solution, and kept in an autoclave in oven at 140 °C for 10 h. The settled solution changed into an emulsion, indicating Sn(OH)₄ had been produced. To remove

the “by-product” (i.e., NH₄Cl) and the remaining ammonia solution, the emulsion was filtered through filter paper for several rounds. Following that, the remaining Sn(OH)₄ was mixed with 15 mL DI water, and kept in water bath at 85 °C for 3 h to evaporate the remaining ammonia and to obtain SnO₂. Afterwards, the as synthesized SnO₂ sol-gel was mixed with ethanol in a volume ratio of 1:5 and ultrasonicated for 30 min to form a colloidal printable ink.

Characterization and Measurements: Various analytical techniques were utilized to characterize the as-synthesized nanoparticles and as-fabricated printable supercapacitors and gas sensors. Morphologies were characterized using field-emission SEM (JSM-7100F, Japan). Chemical compositions were studied by EDS (JSM-7100F, Japan), XPS (PHI 5600, USA), and crystal structures by XRD (Bruker D8 X-ray Diffractometer, USA).

CV measurements based on a two-electrode configuration were performed on an electrochemical workstation (CHI 1000C, USA) at different scan rates of 5, 10, 20, 50, and 100 mV s⁻¹. GCD and EIS measurements based on a two-electrode configuration were performed on an electrochemical workstation (Gamry Instruments, USA). GCD was measured at 0.17, 0.21, 0.30, 0.41, and 0.51 mA cm⁻². EIS was measured with the frequency ranges from 100 kHz to 0.01 Hz with a potential amplitude of 10 mV. Calculations of the areal capacitance and specific power and energy can be found in the Supporting Information.

For the sensor measurement, each sensor was cascaded with a constant resistor and powered by a voltage supplier (V_{dd}). The output voltage was read by a 12-bit analog-to-digital converter, and the resistance of the sensor exposed to different gas environment (R_g) can be calculated through Equation (3)

$$R_g = \frac{V_s}{V_{dd} - V_s} \times R_{cons} \quad (3)$$

where V_s is the voltage drop on the sensor, R_{cons} is the constant resistance in the circuit. The measurements were carried out under room temperature (25 °C) in atmospheric pressure (101.3 kPa). At this point, the saturated vapor pressures for ethanol and acetone are 7.8 and 30.75 kPa, respectively. The flow rates of target gas vapor and carrier gas (i.e., dry air) coming through a bubbler were regulated by two program controlled MFCs (UNIT Instrument, Model UFC-8100). The concentration of the target gas in dry air was controlled through the MFC in different flow rate ratios, namely 1: 4, 2:3, 3:2, 4:1, 5:0, with a total flow rate of 500 sccm. A purging process of 1800 s was performed before the sensor characterization to equilibrate the specimens with dry air. Each gas sensing cycle lasted for 1500 s, including target gas flow last for 600 s and a recovery process with dry air for 900 s.

Supporting Information

Supporting Information is available from the Wiley Online Library or from the author.

Acknowledgements

The authors thank Y. Zhang, Alex H. K. WONG, Christine P. Y. CHEUNG, and Nick K. C. HO from Materials Characterization and Preparation Facility (MCPF), Hong Kong University of Science and Technology for their help on SEM, XRD, and XPS analysis. This work was supported by National Natural Science Foundation of China (project 51672231, 61775091), Shenzhen Key Laboratory Project (SZKLP) (ZDSYS201602261933302), General Research Funds (16237816, 16309018) from Hong Kong Research Grant Council, ITS/415/16, ITS/115/18 from Hong Kong Innovation Technology Commission, The authors also acknowledge the support from Center for 1D/2D Quantum Materials and State Key Laboratory on Advanced Displays and Optoelectronics at HKUST.

Conflict of Interest

The authors declare no conflict of interest.

Keywords

inkjet printing, monolithically integrated self-powered systems, printable gas sensors, printable supercapacitors, wearable and flexible devices

Received: July 6, 2018

Revised: November 2, 2018

Published online:

- [1] W. Gao, S. Emaminejad, H. Y. Y. Nyein, S. Challa, K. Chen, A. Peck, H. M. Fahad, H. Ota, H. Shiraki, D. Kiriya, *Nature* **2016**, 529, 509.
- [2] W. Honda, S. Harada, T. Arie, S. Akita, K. Takeji, *Adv. Funct. Mater.* **2014**, 24, 3299.
- [3] D. Son, J. Lee, S. Qiao, R. Ghaffari, J. Kim, J. E. Lee, C. Song, S. J. Kim, D. J. Lee, S. W. Jun, *Nat. Nanotechnol.* **2014**, 9, 397.
- [4] J. A. Rogers, *Nat. Nanotechnol.* **2017**, 12, 839.
- [5] M. Bariya, H. Y. Y. Nyein, A. Javey, *Nat. Electron.* **2018**, 1, 160.
- [6] M. J. Cima, *Nat. Biotechnol.* **2014**, 32, 642.
- [7] J. Wang, S. Li, F. Yi, Y. Zi, J. Lin, X. Wang, Y. Xu, Z. L. Wang, *Nat. Commun.* **2016**, 7, 12744.
- [8] W. Zeng, L. Shu, Q. Li, S. Chen, F. Wang, X. Tao, *Adv. Mater.* **2014**, 26, 5310.
- [9] Z. Liu, H. Li, M. Zhu, Y. Huang, Z. Tang, Z. Pei, Z. Wang, Z. Shi, J. Liu, Y. Huang, *Nano Energy* **2018**, 44, 164.
- [10] W. Weng, P. Chen, S. He, X. Sun, H. Peng, *Angew. Chem., Int. Ed.* **2016**, 55, 6140.
- [11] Z. Chai, N. Zhang, P. Sun, Y. Huang, C. Zhao, H. J. Fan, X. Fan, W. Mai, *ACS Nano* **2016**, 10, 9201.
- [12] J. Xu, Y. Chen, L. Dai, *Nat. Commun.* **2015**, 6, 8103.
- [13] W. Jia, G. Valdés-Ramírez, A. J. Bando, J. R. Windmiller, J. Wang, *Angew. Chem., Int. Ed.* **2013**, 52, 7233.
- [14] J. Lee, K. Y. Lee, M. K. Gupta, T. Y. Kim, D. Lee, J. Oh, C. Ryu, W. J. Yoo, C. Kang, S. Yoon, *Adv. Mater.* **2014**, 26, 765.
- [15] Z. L. Wang, *Adv. Funct. Mater.* **2008**, 18, 3553.
- [16] M. Zhou, J. Wang, *Electroanalysis* **2012**, 24, 197.
- [17] M. Ha, J. Park, Y. Lee, H. Ko, *ACS Nano* **2015**, 9, 3421.
- [18] Z. Lou, L. Li, L. Wang, G. Shen, *Small* **2017**, 13, 1701791.
- [19] N. A. Kyremateng, T. Brousse, D. Pech, *Nat. Nanotechnol.* **2017**, 12, 7.
- [20] M. R. Lukatskaya, B. Dunn, Y. Gogotsi, *Nat. Commun.* **2016**, 7, 12647.
- [21] G. Yu, X. Xie, L. Pan, Z. Bao, Y. Cui, *Nano Energy* **2013**, 2, 213.
- [22] S. Zheng, J. Ma, Z. Wu, F. Zhou, Y. He, F. Kang, H. Cheng, X. Bao, *Energy Environ. Sci.* **2018**, 11, 2001.
- [23] Z. Zhang, X. Chen, P. Chen, G. Guan, L. Qiu, H. Lin, Z. Yang, W. Bai, Y. Luo, H. Peng, *Adv. Mater.* **2014**, 26, 466.
- [24] F. Zhou, Z. Ren, Y. Zhao, X. Shen, A. Wang, Y. Y. Li, C. Surya, Y. Chai, *ACS Nano* **2016**, 10, 5900.
- [25] X. Xu, S. Li, H. Zhang, Y. Shen, S. M. Zakeeruddin, M. Graetzel, Y. Cheng, M. Wang, *ACS Nano* **2015**, 9, 1782.
- [26] G. Wee, T. Salim, Y. M. Lam, S. G. Mhaisalkar, M. Srinivasan, *Energy Environ. Sci.* **2011**, 4, 413.
- [27] J. Xu, H. Wu, L. Lu, S. Leung, D. Chen, X. Chen, Z. Fan, G. Shen, D. Li, *Adv. Funct. Mater.* **2014**, 24, 1840.
- [28] C. Li, M. M. Islam, J. Moore, J. Sleppy, C. Morrison, K. Konstantinov, S. X. Dou, C. Renduchintala, J. Thomas, *Nat. Commun.* **2016**, 7, 13319.
- [29] J. Yun, Y. Lim, G. N. Jang, D. Kim, S. Lee, H. Park, S. Y. Hong, G. Lee, G. Zi, J. S. Ha, *Nano Energy* **2016**, 19, 401.
- [30] J. Yun, C. Song, H. Lee, H. Park, Y. R. Jeong, J. W. Kim, S. W. Jin, S. Y. Oh, L. Sun, G. Zi, *Nano Energy* **2018**, 49, 644.
- [31] H. Um, K. Choi, I. Hwang, S. Kim, K. Seo, S. Lee, *Energy Environ. Sci.* **2017**, 10, 931.
- [32] Y. Zhong, X. Xia, W. Mai, J. Tu, H. J. Fan, *Adv. Mater. Technol.* **2017**, 2, 1700182.
- [33] R. Xing, Q. Li, L. Xia, J. Song, L. Xu, J. Zhang, Y. Xie, H. Song, *Nanoscale* **2015**, 7, 13051.
- [34] Y. Lin, Y. Gao, F. Fang, Z. Fan, *Nano Res.* **2018**, 11, 3065.
- [35] Z. Wu, X. Feng, H. Cheng, *Natl. Sci. Rev.* **2014**, 1, 277.
- [36] J. Park, M. Kim, Y. Lee, H. S. Lee, H. Ko, *Sci. Adv.* **2015**, 1, e1500661.
- [37] W. Wang, W. Lei, T. Yao, X. Xia, W. Huang, Q. Hao, X. Wang, *Electrochim. Acta* **2013**, 108, 118.
- [38] N. Matsuhisa, M. Kaltenbrunner, T. Yokota, H. Jinno, K. Kuribara, T. Sekitani, T. Someya, *Nat. Commun.* **2015**, 6, 8461.
- [39] H. Pan, Y. Shao, P. Yan, Y. Cheng, K. S. Han, Z. Nie, C. Wang, J. Yang, X. Li, P. Bhattacharya, *Nat. Energy* **2016**, 1, 16039.
- [40] V. Subramanian, H. Zhu, R. Vajtai, P. Ajayan, B. Wei, *J. Phys. Chem. B* **2005**, 109, 20207.
- [41] T. Zhai, X. Lu, F. Wang, H. Xia, Y. Tong, *Nanoscale Horiz.* **2016**, 1, 109.
- [42] Y. Lin, Y. Gao, Z. Fan, *Adv. Mater.* **2017**, 29, 1701736.
- [43] Y. Gao, Y. Lin, J. Chen, Q. Lin, Y. Wu, W. Su, W. Wang, Z. Fan, *Nanoscale* **2016**, 8, 13280.
- [44] A. Brenner, G. E. Riddell, *J. Res. Natl. Bur. Stand.* **1947**, 39, 385.
- [45] D. Wang, Y. Zhang, X. Lu, Z. Ma, C. Xie, Z. Zheng, *Chem. Soc. Rev.* **2018**, 47, 4611.
- [46] Y. Yu, C. Yan, Z. Zheng, *Adv. Mater.* **2014**, 26, 5508.
- [47] M. Beidaghi, Y. Gogotsi, *Energy Environ. Sci.* **2014**, 7, 867.
- [48] Y. Gao, Y. Lin, Z. Peng, Q. Zhou, Z. Fan, *Nanoscale* **2017**, 9, 18311.
- [49] W. Liu, C. Lu, X. Wang, R. Y. Tay, B. K. Tay, *ACS Nano* **2015**, 9, 1528.
- [50] W. Si, C. Yan, Y. Chen, S. Oswald, L. Han, O. G. Schmidt, *Energy Environ. Sci.* **2013**, 6, 3218.
- [51] M. F. El-Kady, R. B. Kaner, *Nat. Commun.* **2013**, 4, 1475.
- [52] W. Shen, *Sens. Actuators, B* **2012**, 166–167, 110.
- [53] J. Chen, Z. Chen, F. Boussaid, D. Zhang, X. Pan, H. Zhao, A. Bermak, C. Tsui, X. Wang, Z. Fan, *ACS Nano* **2018**, 12, 6079.
- [54] A. A. Bokkaf, K. Haddad, J. Fortner, C. S. Lo, P. Biswas, *J. Mater. Chem. A* **2018**, 6, 2053.
- [55] C. Wang, L. Yin, L. Zhang, D. Xiang, R. Gao, *Sensors* **2010**, 10, 2088.
- [56] D. D. Vuong, G. Sakai, K. Shimano, N. Yamazoe, *Sens. Actuators, B* **2004**, 103, 386.
- [57] X. Pan, X. Zhao, J. Chen, A. Bermak, Z. Fan, *Sens. Actuators, B* **2015**, 206, 764.
- [58] X. Pan, X. Liu, A. Bermak, Z. Fan, *ACS Nano* **2013**, 7, 9318.
- [59] A. Mei, X. Li, L. Liu, Z. Ku, T. Liu, Y. Rong, M. Xu, M. Hu, J. Chen, Y. Yang, M. Grätzel, H. Han, *Science* **2014**, 345, 295.
- [60] F. Torrisi, J. N. Coleman, *Nat. Nanotechnol.* **2014**, 9, 738.
- [61] M. Bariya, Z. Shahpar, H. Park, J. Sun, Y. Jung, W. Gao, H. Y. Y. Nyein, T. S. Liaw, L. Tai, Q. P. Ngo, M. Chao, Y. Zhao, M. Hettick, G. Cho, A. Javey, *ACS Nano* **2018**, 12, 6978.
- [62] X. Liu, L. Gu, Q. Zhang, J. Wu, Y. Long, Z. Fan, *Nat. Commun.* **2014**, 5, 4007.
- [63] V. Dua, S. P. Surwade, S. Ammu, S. R. Agnihotra, S. Jain, K. E. Roberts, S. Park, R. S. Ruoff, S. K. Manohar, *Angew. Chem.* **2010**, 122, 2200.